Supporting Information

Bioinspired Wood-Based Wedge-Shaped Surface with Gradient Wettability for Enhanced Directional Liquid Transport and Fog Harvesting

Kaiwen Chen[1, 3], Luyao Chen[1], Xianfu Xiao[1], Cheng Hao[3], Haonan Zhang[2, 3], Tongtong Fu[3], Wei Shang[4], Hui Peng[1], Tianyi Zhan[1], Jianxiong Lyu[1*] and Ning Yan[3*]*

1. Co-Innovation Center of Efficient Processing and Utilization of Forest Resources, College of Materials Science and Engineering, Nanjing Forestry University, Nanjing, 210037, China

2. Jiangsu Provincial Key Lab of Sustainable Pulp and Paper Technology and Biomass Materials, Nanjing Forestry University, Nanjing, Jiangsu Province, 210037, China,

3. Department of Chemical Engineering and Applied Chemistry, University of Toronto, Toronto, Ontario M5S 3B3, Canada

4. College of Chemistry Engineering, Northeast Electric Power University, Jilin 132012, China

Correspondence

E-mail: tyzhan@njfu.edu.cn; jianxiong@caf.ac.cn; ning.yan@utoronto.ca

Figure S1. (a) Digital images and (b) 3-D profiles of PUW and EPW surfaces.

Figure S2. SEM images of cross-section and longitudinal section of PUW and EPW.

Figure S3. Change in contact angle of the sample over 60s.

Figure S4. Tensile properties of samples.

Figure S5. The water absorption and volume change of the samples.

Figure S6. The extend of mold infestation of the samples over 28 days.

Figure S7. The mold infection rate of the samples over 28 days.

Figure S8. Water droplet behavior on the superhydrophilic wedge-shaped wood: (a) Snapshots from video demonstration, (b) Time-resolved dynamic contact angle measurements.

Figure S9. Accumulation of water droplets at the bottom after multiple transport cycles on G3-GWW.

Figure S10. Camera-captured droplet transport behavior on GWW at different inclination angles.

Figure S11. Final transport distances of droplets with varying volumes on G3-GWW (wedge angle: 9°) at different inclination angles.Figure S9. The weight and frequency of water droplets detaching from individual fog-harvesting units within the fog-driven power device.

Figure S12. The weight and frequency of water droplets detaching from individual fog-harvesting units within the fog-driven power device.

Figure S13. Fog harvesting performance of an array-type cactus spine and gradient wettability wedge-shaped wood collector.

Table S1. Definition of the three simulation cases and their constant versus variable parameters.

Table S2. Interpretation for the three scenarios.

Table S3. A performance comparison with other materials capable of achieving unidirectional liquid transport.

Table S4. Comparison of fog collection efficiencies and surface designs in representative bioinspired fog-harvesting systems.

Supplementray Video 1. Droplet transport comparison on G1–G3 GWW surfaces (side view, contact angle system).

Supplementray Video 2. Droplet transport comparison on G1–G3 GWW surfaces (camera view).

Supplementray Video 3. Droplet transport on GWW with 5°, 9°, and 15° wedge angles (side view, contact angle goniometer)

Supplementray Video 4. Droplet transport on GWW with 5°, 9°, and 15° wedge angles (camera view)

Supplementray Video 5. Inclination-induced droplet transport on GWW surfaces (camera view)

Supplementray Video 6. The application of fog-driven power devices.

Materials and Methods

1. Resin Solutions for Preparing Comparison Samples:

Polyurethane Resin (PU): A waterborne polyurethane resin with a solid content of 45% was used without further modification.

Epoxy Resin (EP): An E51 epoxy resin was prepared by mixing the resin with its curing agent at a weight ratio of 1:1 to form the epoxy resin solution.

2. Resin Impregnation of Delignified Wood as Comparison Samples:

The delignified wood (DW) samples were separately impregnated with the prepared polyurethane (PU) and epoxy resin (EP) solutions through a vacuum-assisted process. The samples were placed in the respective resin solutions under a vacuum pressure of 0.1 MPa for 3 hours to ensure thorough infiltration of the resin into the wood matrix. This methodology ensured uniform resin impregnation, providing a robust foundation for subsequent material characterization and analysis.

3. Anti-mildew performance test

First, seal samples with dimensions of 50 × 20 × 1 mm^3 in bags and subject them to high-pressure sterilization at 120°C for 6 hours. After sterilization, transfer the samples to sterile Petri dishes in a clean room and inoculate them with Aspergillus niger spores. Place the Petri dishes in an incubator set at 65°C and 25% humidity for one month. Monitor and record the growth of Aspergillus niger every two days.

To better validate the superior structure and performance of PVDF-HFP-impregnated wood (PW), additional comparison samples of polyurethane resin-impregnated wood (PUW) and epoxy resin-impregnated wood (EPW) were prepared. As shown in Figure

S1, PUW and EPW surfaces were flat, with no visible groove structures **(Figure S1**). SEM images (**Figure S2**) revealed that the cell walls of earlywood and latewood in PUW and EPW were fully filled with resin, and the tracheid walls in the longitudinal sections were similarly covered, completely blocking the natural pore structure of the wood. Although this filling increased the structural density of the wood, it significantly limited its microchannel characteristics, thereby inhibiting directional liquid transport. In comparison, PW exhibited superior wettability, likely due to the surface modification properties of PVDF-HFP and its uniform pore filling (**Figure S3**). In terms of mechanical properties, although EPW demonstrated the highest tensile strength (44.8 MPa), PW achieved a tensile strength of 35.1 MPa, which was 1.2 times and twice as high as PUW and DW, respectively (**Figure S4**). This indicated that PVDF-HFP impregnation not only improved the structural compactness of the wood but also significantly enhanced its mechanical properties while maintaining a degree of flexibility. Conversely, the lower tensile strength of PUW and DW could be attributed to the lower hardness of polyurethane and the structural degradation caused by delignification, respectively.

Natural wood (NW) exhibited moderate water absorption and volume expansion due to its inherent microstructure. Delignified wood (DW), with increased porosity following lignin removal, showed significantly higher water absorption and volume changes (**Figure S5**). In contrast, PW demonstrated a balanced performance, with slightly higher water absorption than NW but significantly lower than DW, along with reduced volume expansion. This suggested that PVDF-HFP effectively reduced water

absorption and inhibited swelling. Compared to PUW and EPW, PW achieved a balance between water absorption and volume stability. Its moderate water absorption helped to maintain flexibility while substantially minimizing water-induced swelling. After a 28-day antifungal test, the infection rates of NW, DW, and PW were 10%, 33%, and 1%, respectively (**Figure S6** and **S7**), indicating PW's superior antifungal performance. This advantage likely stemed from the filling effect of PVDF-HFP, which blocked the pathways for water and nutrients essential for microbial growth. In contrast, DW, with its high porosity and water absorption, provided an ideal environment for microbial proliferation, resulting in the highest infection rate. Although NW retained some natural defense mechanisms, it was still inferior to the protection offered by the PVDF-HFP impregnation.

4. Theoretical correlation between interfacial curvature and spreading velocity of droplets

A quantitative theoretical model was established to couple the evolution of interfacial curvature with the instantaneous spreading velocity U of droplets moving along wedge-shaped surfaces endowed with wettability gradients. The formulation encompasses all three experimental conditions investigated in this study: (i) a fixed wedge angle with different wettability gradients, (ii) a fixed gradient with different wedge angles, and (iii) a fixed geometry/gradient under various inclination angles.

Table S1. Definition of the three simulation cases and their constant versus variable parameters.

Scenario	Constant parameters	Variable parameters
Case 1	wedge angle $\alpha = 9°$	Wettability gradients G1, G2, G3
Case 2	Wettability gradients = G3	α = 5°, 9°, 15°
Case 3	Wettability gradients = G3, α = 9°	Inclination angle β = 0° – 90°

4.1 General force balance

For a droplet of volume V and viscosity μ, the contact-line velocity is governed by a balance between driving forces and viscous resistance (Stokes regime):

$$k\mu U = F_L + F_W - F_g \tag{S1}$$

where

- F_L – Laplace-pressure force arising from curvature gradients;
- F_W – capillary force due to the spatial variation of surface free energy;
- Fg – gravitational component opposing motion when the substrate is tilted;
- k – geometry-dependent constant (≈ 3π for a spherical-cap droplet).

4.2 Laplace-pressure contribution F_L

Along the wedge axis (coordinate x), the local principal radius of curvature of the advancing front is:

$$R(x) = \frac{h(x)}{\sin\varphi} \approx \frac{x\tan\alpha}{\sin\varphi} \tag{S1}$$

(φ is the azimuthal angle of the meniscus). The Laplace pressure difference between the advancing (a) and receding (r) edges is

$$\Delta P = \sigma\left(\frac{1}{Ra} - \frac{1}{R_r}\right) \approx \sigma\frac{\Delta x}{R^2(x)} \tag{S2}$$

So that

$$F_L = A\Delta P \propto \frac{\sigma \Delta x}{R^2(x)} \propto \frac{\sigma}{x^2} \tag{S3}$$

indicating that the driving force—and hence U—increases rapidly as the droplet moves into regions of higher curvature (smaller x).

4.3 Wettability-gradient contribution F_W

With a linear contact-angle profile $\theta(x) = \theta_0 - \nabla\theta_x$ (G1–G3), the differential capillary force along the contact line of length L is:

$$F_w = \gamma L\left[\cos\theta_{rec}(x) - \cos\theta_{adv}(x + \Delta x)\right] \approx -\gamma L \nabla\theta \sin\theta(x) \tag{S4}$$

Thus F_W scales with the contact-angle gradient ∇θ; G3 (steepest gradient) yields the largest F_W.

4.4 Gravitational term F_g (inclined substrates)

For a tilt angle β relative to the horizontal,

$$F_g = \rho v g \sin\beta \tag{S5}$$

acts opposite to the spreading direction.

4.5 Unified velocity expression

Substituting Eqs. (2–4) into Eq. (1) gives

$$U(x,a,\nabla\theta,\beta) = \frac{1}{k\mu}\left[\frac{c_1\sigma}{x^2 \tan^2\alpha} + C_2\gamma\nabla\theta\sin\theta(x) - \rho V g \sin\beta\right] \tag{S6}$$

where $C_{1,2}$ absorb geometric factors. Equation (5) explicitly links local curvature (x−2), wedge geometry (tanα), wettability gradient ($\nabla\theta$), and inclination (β) to the instantaneous spreading speed.

Table S2. Interpretation for the three scenarios.

Scenario	Dominant term(s) in Eq. (5)	Predicted trend	Simulation / experiment
Case 1 (G1→G3)	Wettability term $\propto\nabla\theta$	$U_{G3} > U_{G2} > U_{G1}$	Confirmed: 7.6 mm s^{-1} (G3) > 5.1 mm s^{-1} (G2) > 2.4 mm s^{-1} (G1)
Case 2 (α)	Curvature term $\propto 1/\tan^2\alpha$	U5° > U9° > U15°	Confirmed: peak U 8.9 mm s^{-1} at 5°
Case 3 (β)	Gravity term $\propto \sin\beta$	U decreases monotonically with β	Confirmed: 5.6 mm s^{-1} at 0° → 0.64 mm s^{-1} at 90°

4.6 Implications

Equation (5) reveals two practical levers for accelerating directional transport: (i) sharpening the curvature gradient by reducing α or shortening x; and (ii) steepening the surface-energy gradient (larger ∇θ). Conversely, substrate tilting introduces a gravitational penalty that must be offset by either lever. These insights rationalise the design choices adopted in this study and provide predictive guidelines for future gradient-surface architectures.

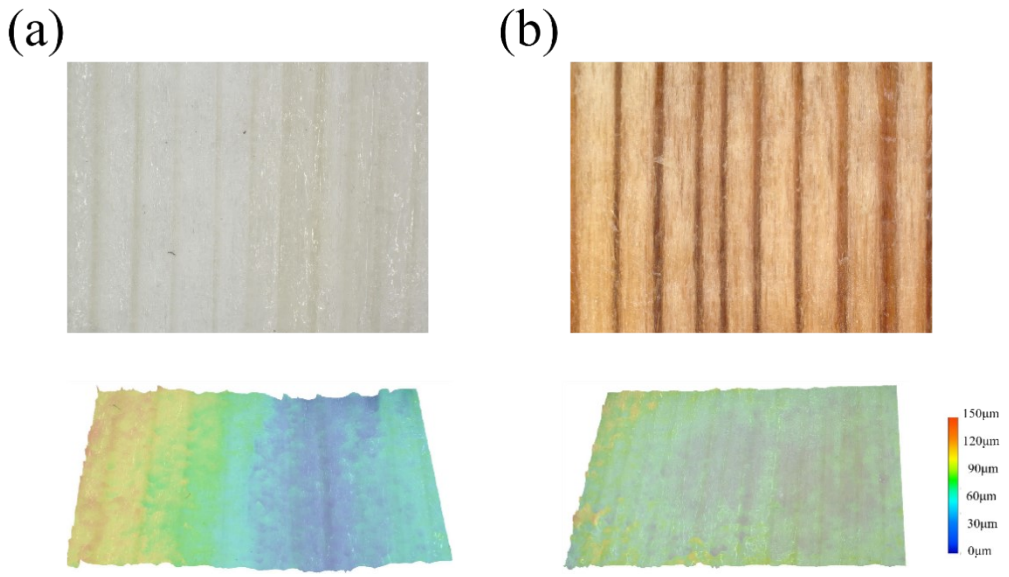

Figure S1. (a) Digital images and (b) 3-D profiles of PUW and EPW surfaces.

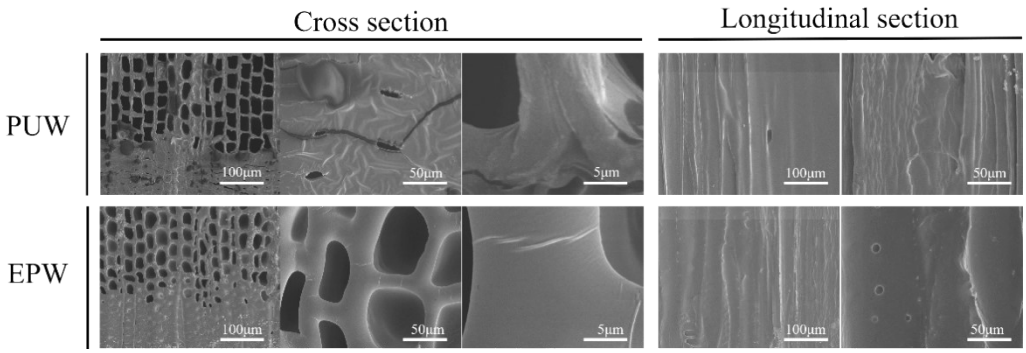

Figure S2. SEM images of cross-section and longitudinal section of PUW and EPW.

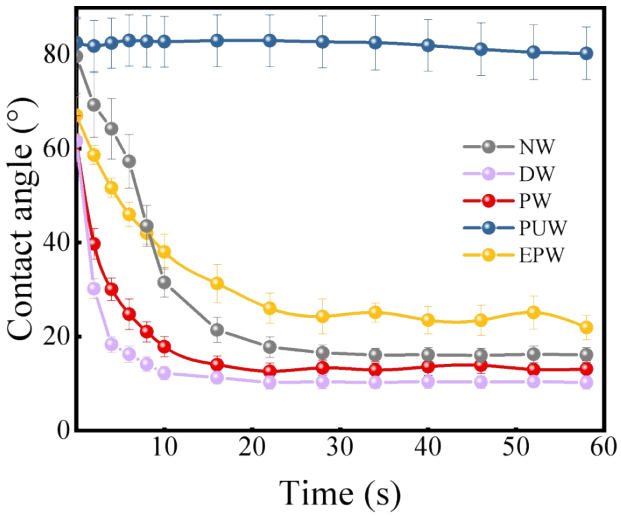

Figure S3. Change in contact angle of the sample over 60s.

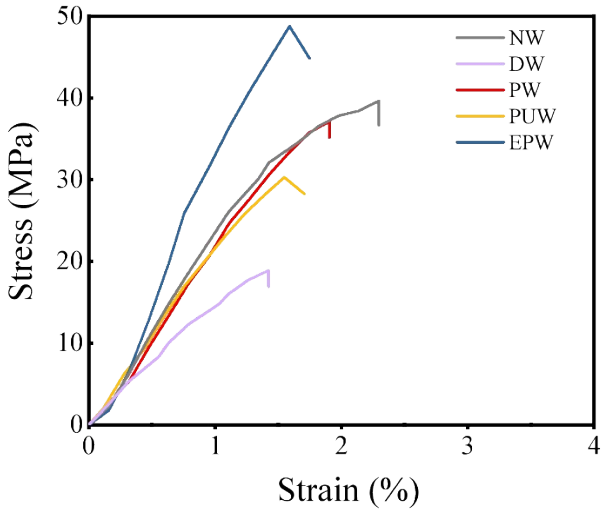

Figure S4. Tensile properties of samples.

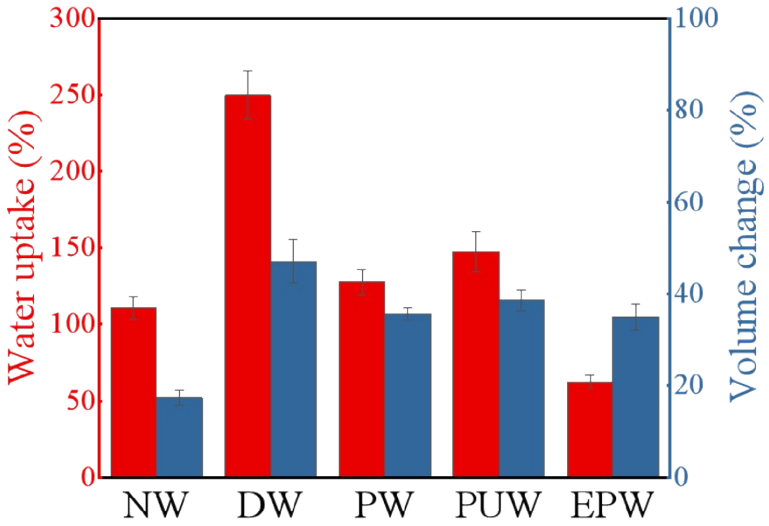

Figure S5. The water absorption and volume change of the samples.

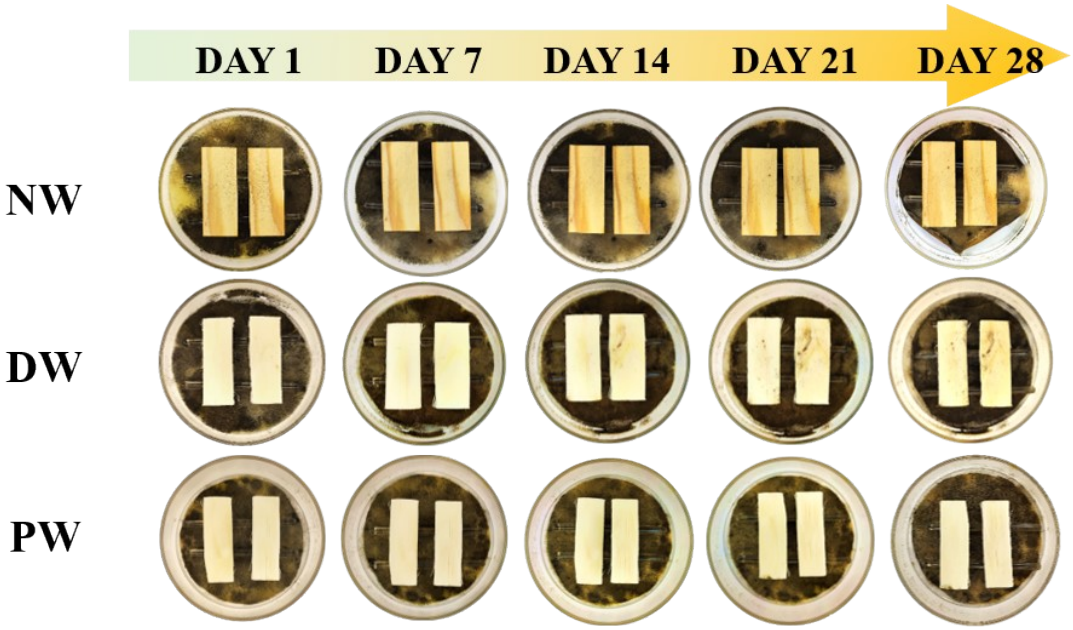

Figure S6. The extend of mold infestation of the samples over 28 days.

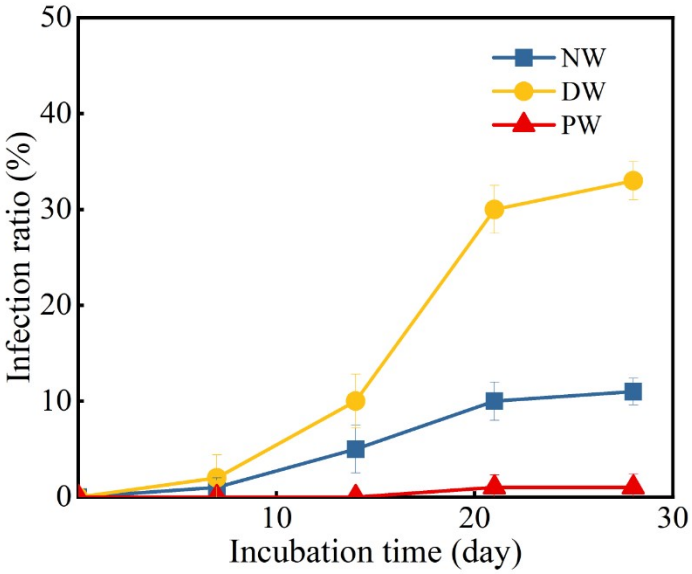

Figure S7. The mold infection rate of the samples over 28 days.

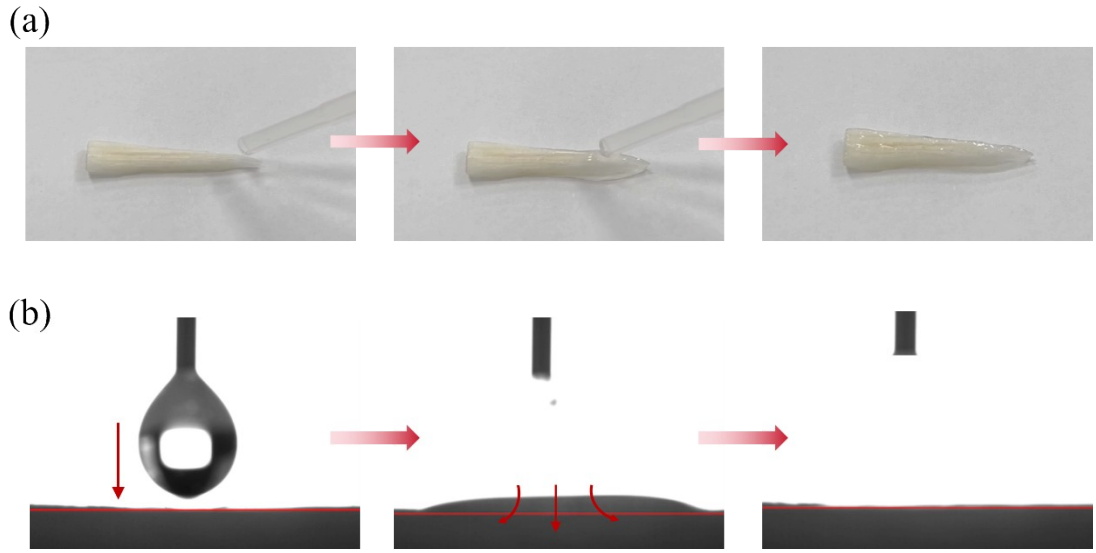

Figure S8. Water droplet behavior on the superhydrophilic wedge-shaped wood: (a) Snapshots from video demonstration, (b) Time-resolved dynamic contact angle measurements.

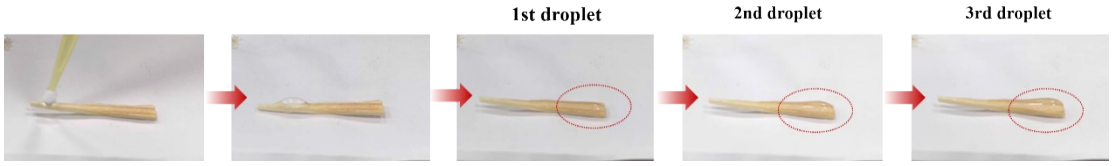

Figure S9. Accumulation of water droplets at the bottom after multiple transport cycles on G3-GWW.

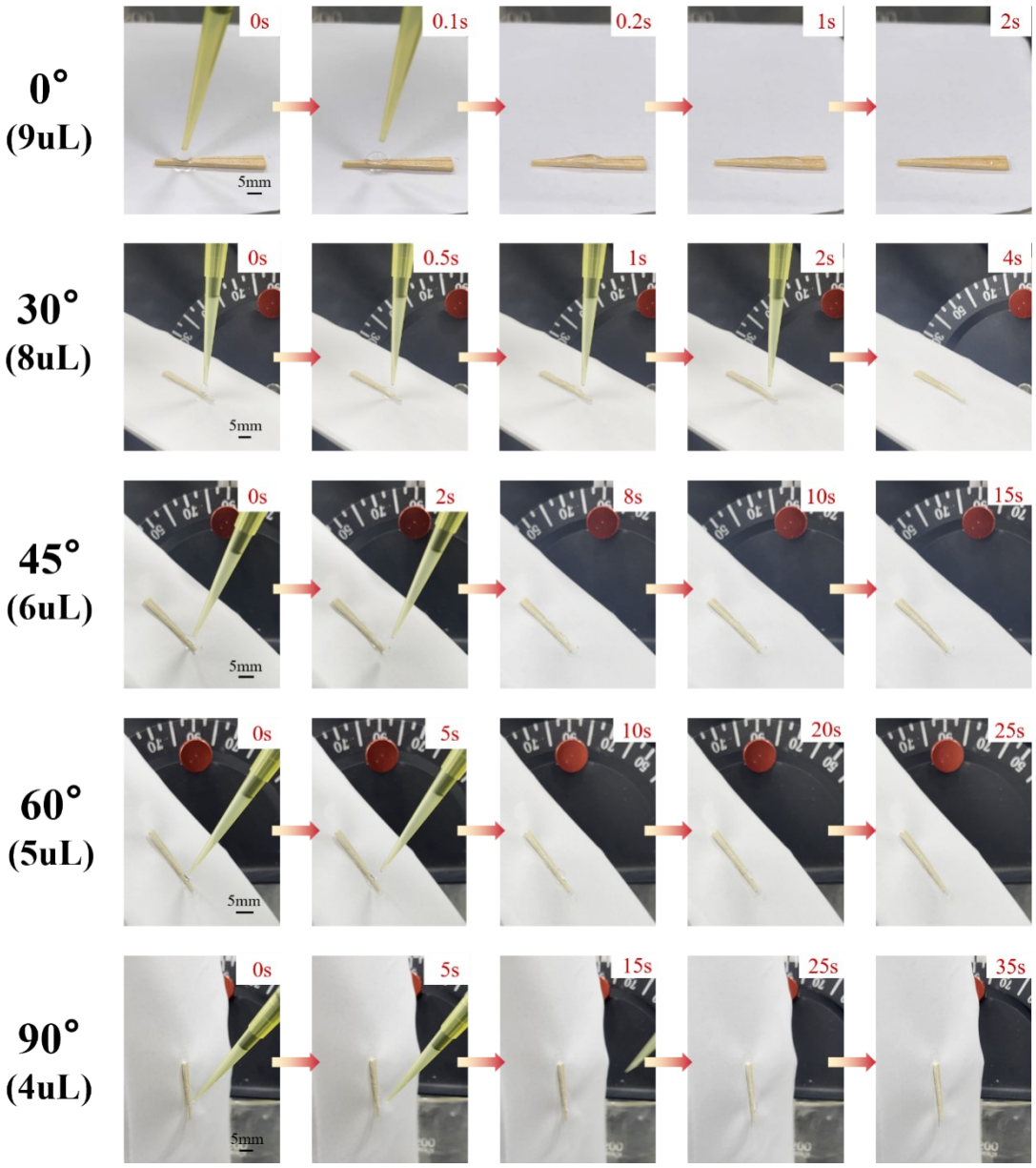

Figure S10. Camera-captured droplet transport behavior on G3-GWW at different inclination angles.

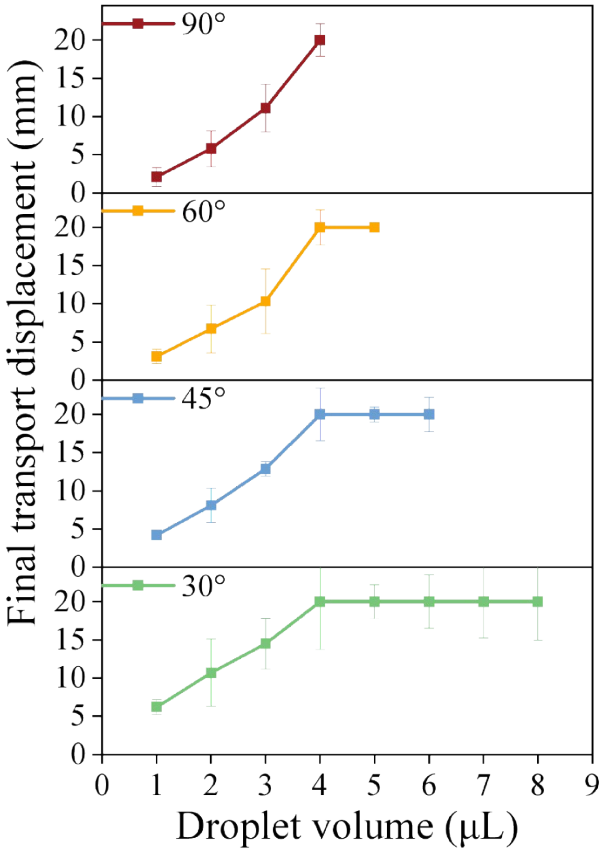

Figure S11. Final transport distances of droplets with varying volumes on G3-GWW (wedge angle: 9°) at different inclination angles.

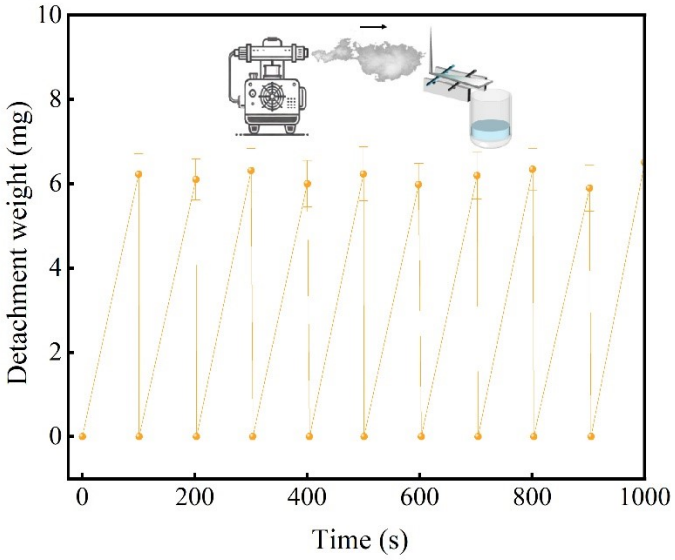

Figure S12. The weight and frequency of water droplets detaching from individual fog-harvesting units within the fog-driven power device.

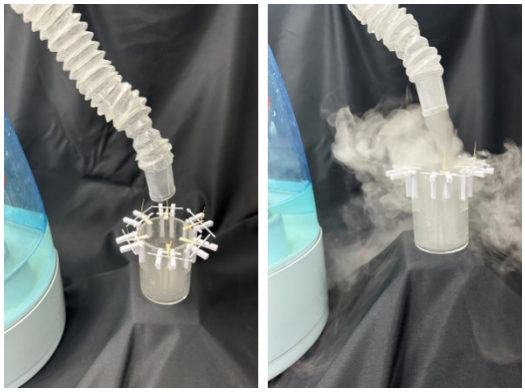

Figure S13. Fog harvesting performance of an array-type cactus spine and gradient wettability wedge-shaped wood collector.

Table S3. A performance comparison with other materials capable of achieving unidirectional liquid transport.

Material	Structural design	Fabrication method	Liquid unidirectional transport rate (mm/s)	Refs.
Photopolymerized resin (Veroclear-RGD 810)	Dual-scale island arrays	Digital light processing three-dimensional printing technology	4-6	[1]
Poly(methyl methacrylate)	Biomimetic scale-like structure	Laser engraving	1	[2]
Graphite plate	Wedge pattern with gradient wettability	Anodic oxidation method	3.5	[3]
Ag/Cu surfuce	Wedge pattern with gradient wettability	Gradient displacement reaction	0.53	[4]
photoresponsive thiol–yne photopolymer	Wedge pattern with gradient wettability	Asymmetric UV radiation	0.85-1.25	[5]
Modified titanium dioxide (TiO_2)-based coatings	Single channel with gradient wettability	Photolithography	~1.8	[6]
Wood	Wedge-shaped surface with gradient wettability	chemical treatment and UV-induced modification	8.9	Our work

Table S4. Comparison of fog collection efficiencies and surface designs in representative bioinspired fog-harvesting systems.

Material	Structural design	Fabrication method	Fog collection rate ($kg/m^2 \cdot h$)	Refs.
Sticky paper and aluminum (Al) alloy	A hybrid superhydrophobic–hydrophilic pattern	Mechanical drilling, coating, chemical modification, bonding,	3.63	[7]
Titanium alloy	Laser grid texturing with varied texturing intervals (TI)	Laser ablation and silicone oil heat treatment	4.2	[8]
Brass (H59) sheets	Superhydrophobic/hydrophilic pattern arrays	Laser ablation and heat treatment	4.3	[9]
Aluminum (Al) alloy sheet	Bionic pattern of honeycomb and cactus spine coupling	Electrochemical etching, FAS modification, Nanosecond laser etching	0.967-1.06	[10]
Copper sponge	3D interconnected porous skeleton	Chemical corrosion and PDMS modification	0.03	[11]
Glass	Interconnected microchannels	Laser ablation and Chemical vapor deposition	~0.07	[12]
Wood and cactus spine	Six functional collection units	Chemical treatment and UV-induced modification	7.2	Our work

References:

1. Y. Si, T. Wang, C. Li, C. Yu, N. Li, C. Gao, Z. Dong and L. Jiang, *ACS Nano*, 2018, **12**, 9214-9222.
2. G. Buchberger, R. Baumgartner, A. Kogler, T. Fritz, S. Bauer and W. Baumgartner, *Sensors and Actuators A: Physical*, 2018, **283**, 375-385.
3. S. Deng, W. Shang, S. Feng, S. Zhu, Y. Xing, D. Li, Y. Hou and Y. Zheng, *Scientific Reports*, 2017, **7**, 45687.
4. Y. Li, J. Huang, J. Cheng, S. Xu, P. Pi and X. Wen, *ACS Applied Materials & Interfaces*, 2021, **13**, 15857-15865.
5. E. Rossegger, D. Hennen, T. Griesser, I. Roppolo and S. Schlögl, *Polymer Chemistry*, 2019, **10**, 1882-1893.
6. H. Wu, K. Zhu, B. Cao, Z. Zhang, B. Wu, L. Liang, G. Chai and A. Liu, *Soft Matter*, 2017, **13**, 2995-3002.
7. R. Sun, J. Zhao, C. Liu, N. Yu, J. Mo, Y. Pan and D. Luo, *Progress in Organic Coatings*, 2022, **171**, 107016.
8. S. Liu, C. Sun, K. Zhang, Y. Geng, D. Yu and C. Wang, *Optics & Laser Technology*, 2024, **172**, 110523.
9. J. Gao, Y. Song, L. Huang, H. Luo, X. Dong, C. Wang and J.-a. Duan, *Langmuir*, 2023, **39**, 18143-18151.
10. X. Li, G. Zhang, K. Du, S. Yin, Y. Liu, X. Xu and Y. Liu, *Chemical Engineering Journal*, 2024, **497**, 154728.
11. K. Deng, X. Zhang, B. Yuan, Z. Deng, X. Liu and B. Shang, *Journal of Environmental Chemical Engineering*, 2022, **10**, 108771.
12. Y. Wang, Y. Zhou, P. Han, G. Qi, D. Gao, L. Zhang, C. Wang, J. Che, Y. Wang and S. Tao, *Environmental Science & Technology*, 2024, **58**, 3812-3822.